Proceedings of the Combustion Institute 42 (2026) 106041

Contents lists available at ScienceDirect

Proceedings of the Combustion Institute

journal homepage: www.elsevier.com/locate/proci

Effect of magnetic force on intrinsic instabilities in lean hydrogen flames

Vaibhav Mysore Natesh *, Ivan Langella

Faculty of Aerospace Engineering, TU Delft, Kluyverweg 1, Delft, 2629 HS, The Netherlands

ARTICLE INFO

Keywords:
Magnetic fields
Intrinsic flame instabilities
Hydrogen flames

ABSTRACT

Controlling intrinsic flame instabilities in lean premixed hydrogen flames is central to stable, efficient, and low-emission operation. This study assesses whether steady magnetic-field gradients can be used to control the growth of intrinsic flame instabilities. For this purpose, two-dimensional high-fidelity laminar simulations are performed for a lean hydrogen-air flame, with full chemistry and constant magnetic-field gradients applied along and against the streamwise direction. A linear stability analysis is first carried out to examine how the imposed magnetic forcing modifies perturbation growth through the corresponding dispersion relation. The analysis shows that a negative streamwise magnetic-field gradient weakens the long-wavelength branch associated with hydrodynamic instability. The nonlinear flame dynamics are then examined, showing that when the magnetic-field gradient is applied opposite to the flow, global flame wrinkling is reduced by about 22% at $|\nabla(B^2)| = 3000\,\mathrm{T^2\,m^{-1}}$, while the stretch factor and the super-adiabatic temperature remain nearly unchanged. Moreover, it is observed that the magnetic gradient triggers the generation of counter-rotating vortical structures that oppose the Darrieus-Landau instability, while the thermodiffusive instability remains unaffected. The mechanism underlying this behaviour is explained in the paper. Magnetic fields thus offer a contactless means to modulate instability growth in premixed hydrogen flames and provide a physics-based framework for future stability control strategies.

Novelty and significance statement: This work demonstrates, for the first time, the use of magnetic-field gradients to control the growth of intrinsic flame instabilities (IFI) in lean premixed hydrogen flames. It identifies the hydrodynamic (Darrieus–Landau) mode as the instability suppressed by the forcing and explains the mechanism responsible for this response. The underlying physics remains largely unexplored, yet it is directly relevant to next-generation hydrogen combustors where instability control is a key requirement. The results help identify a relevant gradient range and indicate effective in-flame placement strategies for targeted experiments and early design studies.

1. Introduction

Hydrogen has gained significant attention as a fuel in recent years because it enables carbon-free combustion and can be produced from renewable energy. Its high reactivity also supports ultra-lean premixed operation, which reduces peak flame temperature and helps limit the production of nitrogen oxides (NO_x) [1]. However, lean premixed hydrogen flames are prone to intrinsic flame instabilities (IFI), which can lead to strong flame wrinkling and potentially undesirable unsteady dynamics [2]. Achieving robust control of IFI is therefore an enabling requirement for next-generation hydrogen combustors.

In the present context, IFI is governed by two mechanisms. The first is the hydrodynamic Darrieus–Landau instability (DLI), which is driven by the gas expansion across the flame and the resulting density jump that promotes corrugation growth. The second is the thermodiffusive instability (TDI), which originates from preferential diffusion associated with hydrogen. In lean hydrogen flames, these mechanisms can coexist and act synergistically, producing substantial enhancements of global fuel consumption speed relative to an unperturbed planar flame. Recent analyses have shown that such nonlinear regimes yield propagation speeds up to 4 times the corresponding laminar flame speed [3]. This sensitivity highlights the need for control strategies that can selectively alter the instability growth mechanisms while preserving the underlying flame structure.

Although several control concepts have been developed to mitigate unsteady behaviour in lean premixed combustors, these have mainly targeted thermoacoustic oscillations. Active approaches based on pressure or heat-release feedback, acoustic forcing, and fuel-flow modulation have been shown to reduce limit-cycle amplitudes, but their effectiveness depends on sensing and actuation quality, controller tuning, and robustness across operating conditions [4,5]. Plasma-based

* Corresponding author.
E-mail address: v.mysorenatesh@tudelft.nl (V.M. Natesh).

https://doi.org/10.1016/j.proci.2026.106041
Received 15 March 2026; Accepted 5 June 2026
Available online 24 June 2026

actuation offers a different route by depositing energy and generating radicals on short timescales, thereby modifying ignition and flame response, although practical implementation remains challenging because of integration complexity, power requirements, and durability [6–8]. Passive measures such as swirl, confinement, and damping hardware are also common, but they primarily target combustor-scale feedback mechanisms sustaining thermoacoustic modes [5,9]. By contrast, studies specifically addressing the control of IFI remain limited.

In contrast, intrinsic flame instabilities arise from local flame–transport–flow coupling and can persist even when acoustic feedback is weak. Prior efforts to influence the thermodiffusive instability have been focused primarily on modifying the local flame environment. In particular, recent numerical work has shown that increasing strain rate can damp perturbation growth and suppress unstable flame-front dynamics in lean premixed hydrogen flames [10]. Liquid-water injection has also been explored as a means of altering intrinsic-instability development through coupled thermal, diffusive, and flow-field effects, although its influence is not unconditionally stabilising and can also enhance flame wrinkling depending on the configuration and droplet conditions [11,12]. This gap motivates the use of a fundamentally different, contactless mechanism, in which an imposed magnetic-field gradient modifies the near-flame flow environment and thereby influences instability growth.

In flames subjected to an externally imposed non-uniform magnetic field, the magnetic interaction is primarily mediated by paramagnetic species, most notably oxygen, which experience volumetric body forces through magnetisation [13]. In addition, magnetic forcing can induce a relative drift of paramagnetic species with respect to the bulk flow [13]. These effects can modify local scalar gradients and momentum coupling, and thereby influence wrinkling, heat release, and stabilisation. Most prior studies have focused on laminar diffusion flames [13–16], where the magnetic field was observed to act mainly on oxygen on the oxidiser side, which in turn alters the bulk flow and consequently the flame structure and species distribution. In contrast, the influence of magnetic fields on premixed configurations has received limited attention since the direct effect on chemistry and species transport is weak [17], in contrast to plasma-assisted combustion or charged-species formulations, where electromagnetic effects can act more directly on the reaction zone. However, magnetic forcing can still influence the flame indirectly by reshaping the velocity field through the associated body force, thereby modifying the near-front strain field. This is especially relevant for lean premixed hydrogen flames, where non-unity Lewis-number effects and differential diffusion couple strongly with strain and curvature [18]. As a result, magnetic forcing can alter instability growth and front wrinkling even when its direct effect on chemistry remains weak.

In our earlier study [19] of a lean premixed swirl-stabilised hydrogen flame, magnetic forcing was shown to interact with differential diffusion and strain and to be effective in lowering peak temperature and heat-release rate. This motivates the present study, where the magnetic field is evaluated in its potential to control the growth of intrinsic instabilities in premixed hydrogen flames. The objective of the present work is thus to investigate whether and how magnetic fields affect IFI in lean premixed hydrogen flames. A linear stability analysis is first performed to determine how an imposed constant magnetic gradient modifies perturbation growth through the corresponding dispersion relation. The analysis is then extended to the fully developed regime by quantifying changes in flame wrinkling and consumption speed with and without magnetic forcing. Finally, the relative influence of the magnetic field on the DLI and TDI is examined, and the physical mechanism underlying the observed response is discussed.

2. Methodology

2.1. Modelling

The reactive Navier–Stokes equations for mass conservation, momentum, energy and species transport [9] are modified to account for the effect of the magnetic body forces. The external magnetic force acting on a paramagnetic species i is modelled as a mass-specific Kelvin term,

$$f_i \ = \ \frac{\chi_i}{2\,\mu_0}\,\nabla\!\left(B^2\right), \tag{1}$$

where f_i is the force per unit mass, μ_0 is the vacuum permeability, χ_i is the magnetic susceptibility of species i, and B is the magnetic flux density. Lorentz force and Hall drift effects on charged species are neglected here. This approximation is supported by the low charged-species concentrations typically reported in hydrogen flames, by previous magnetostatic reacting-flow studies in which weak current-density effects were neglected compared with magnetic forcing of neutral paramagnetic species [20–22], and by earlier magnetic-flame studies showing that Lorentz-force effects were considerably smaller than magnetic-gradient forcing and did not significantly affect flame deformation [23]. The present formulation is therefore restricted to a two-dimensional magnetostatic Kelvin-force framework. If charged-species electrodynamics were to be retained, a fully three-dimensional treatment would become important because additional out-of-plane coupling terms could then influence the detailed instability dynamics.

The temperature dependence of magnetic susceptibility is described by Curie's law [13]:

$$\chi_i = \frac{N_A g_L^2 \mu_B^2 S_i(S_i+1)\mu_0}{3kT m_i} \tag{2}$$

where N_A is Avogadro's number, g_L is the Landé g-factor accounting for the coupling between an electron's spin and the applied magnetic field, μ_B is the Bohr magneton representing the fundamental unit of magnetic moment associated with an electron, S_i is the total electron spin quantum number of species i which determines its intrinsic magnetic moment, μ_0 is the vacuum permeability describing the ability of free space to support a magnetic field, k is the Boltzmann constant relating temperature to energy at the molecular scale, T is the absolute temperature which inversely affects the magnetic susceptibility, and m_i is the molecular mass of species i influencing the strength of its magnetic response.

The magnetic-field coupling is introduced through additive terms in the governing equations. In the momentum equation, the magnetic body force per unit volume is written as

$$F_m = \rho \sum_{i=1}^{N_s} Y_i\, f_i. \tag{3}$$

where N_s is the total number of species, ρ is the density of the mixture, and Y_i is the mass fraction of species i. In the species transport equations, the total diffusive flux of species i is written as

$$\mathbf{J}_i \ = \ \rho Y_i \mathbf{V}_i \ = \ \mathbf{J}_i^F \ + \ \mathbf{J}_i^m \ + \ \mathbf{J}_i^T, \tag{4}$$

where V_i is the diffusion velocity of species i, $\mathbf{J}_i^F$ is the Fickian contribution driven by composition gradients, $\mathbf{J}_i^m$ is the magnetic-field-induced contribution associated with differential Kelvin forcing, and $\mathbf{J}_i^T$ is the thermal-diffusion (Soret) contribution. The Fickian term is

$$\mathbf{J}_i^F = -\rho D_i \, \nabla Y_i. \tag{5}$$

The magnetic contribution follows from the force-driven part of the diffusion-velocity closure and is expressed as

$$\mathbf{J}_i^m = \rho D_i \, \frac{m_i}{m} \frac{\rho}{p} \sum_{j=1}^{N_s} Y_i Y_j \left(\mathbf{f}_i - \mathbf{f}_j\right), \tag{6}$$

where p denotes the pressure and m the mixture molecular mass. Species with different $\mathbf{f}_i$ therefore experience a relative drift in the presence of a magnetic-field gradient. Finally, the thermal-diffusion (Soret) contribution is written as

$$\mathbf{J}_i^T = -\rho \mathcal{D}_{T,i} \frac{\nabla T}{T}, \tag{7}$$

where $\mathcal{D}_{T,i}$ is the thermal-diffusion coefficient for species i.

A magnetic work term W_m is also added to the sensible enthalpy transport equation, and it is written as

$$W_m = \rho \sum_{i=1}^{N_s} Y_i f_i \cdot V_i. \tag{8}$$

A correction velocity is applied to ensure that the total diffusive mass flux satisfies $\sum_{i=1}^{N_s} J_i = 0$ after including J_i^m. Full expressions and implementation details for the reacting-flow equations with magnetic-field coupling are provided in our prior work [19,24].

2.2. Computational details

Two-dimensional laminar simulations of freely-propagating flames are carried out in a rectangular domain (see Fig. 1) in both the linear [25,26] and nonlinear regimes [27]. The stream of reactants enters the domain from the left with a uniform velocity U_0 and the burnt gases exit the domain from the right. Periodic boundary conditions are imposed in the transverse direction. The setup follows the approach of Berger et al. [27]. The reactants consist of a mixture of hydrogen and air at equivalence ratio $\phi = 0.4$, unburned temperature $T_u = 300$ K, and pressure $p = 1$ atm. The inlet speed U_0 and the domain length L_x are chosen so that the flame remains within the computational domain for a statistically meaningful time. To avoid lateral confinement effects, the transverse width is set to $L_y > 100\,\delta_f$, where δ_f is the laminar thermal thickness. This choice is consistent with the domain-independence guidance reported by Berger et al. [28].

The reacting flow is modelled using the reacting Navier–Stokes equations in the low Mach number limit for an ideal gas. The governing equations are discretised using an *in-house* version of reactingFOAM that includes the magnetic source terms described in Section 2.1. Spatial derivatives are discretised using central differencing schemes, while a TVD scheme is used for the divergence term in the momentum equation to improve stability in the flame region. Time integration is performed with a first-order implicit Euler scheme, and the time step is chosen to keep the maximum Courant number below 0.2. The chemical mechanism of Burke et al. [29] is used to model the chemistry.

Species diffusion is treated as Fickian with constant molecular diffusivities, defined as $D_i = \lambda/(\rho c_p Le_i)$, where λ is the thermal conductivity, ρ the density, c_p the specific heat of the mixture at constant pressure, and Le_i the spatially uniform Lewis numbers taken from the burnt-gas region of corresponding one-dimensional freely propagating laminar flame calculations. This choice follows the constant-Le framework used by Berger et al. [3] for lean premixed hydrogen intrinsic-instability studies, where it was found to provide a good approximation of the unstretched laminar flame speed. While a more detailed mixture-averaged transport model [30] would refine the quantitative description, the present framework is sufficient to identify the main trends associated with the imposed magnetic forcing and to maintain consistency with prior lean-hydrogen intrinsic-instability studies. Thermal diffusion (Soret effect) is included via the Bartlett formulation [31].

Magnetic forcing is introduced by imposing a constant streamwise gradient of B^2, with $\nabla(B^2)$ oriented either in the $+x$ or in the $-x$ direction. In addition to the baseline configuration where both Darrieus–Landau (DLI) and thermodiffusive (TDI) mechanisms are active, a second set of simulations, considered in the nonlinear regime, isolates the DLI by suppressing the TDI by setting $\mathrm{Le}_i = 1$ for all species. A reference case without magnetic forcing was also performed. For cases with both instability mechanisms present, two gradient magnitudes are considered, $|\nabla(B^2)| = 2000$ and 3000 $\mathrm{T}^2\,\mathrm{m}^{-1}$. For the

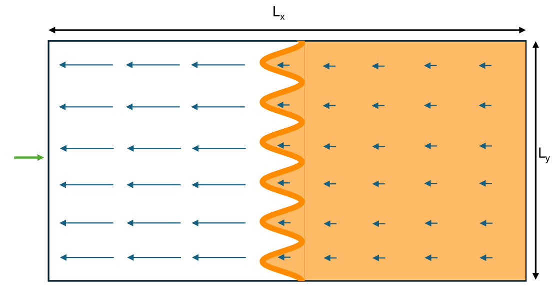

Fig. 1. 2D computational domain showing the initial perturbation of the flame. Blue arrows indicate magnetic force lines, and the green arrow indicates the inlet.

unity-Lewis-number configuration, two smaller magnitudes are used, $|\nabla(B^2)| = 1000$ and 2000 $\mathrm{T}^2\,\mathrm{m}^{-1}$, because comparable responses are obtained with weaker gradients when thermodiffusive effects are removed. Note that a gradient is needed to observe any effect on the flame because the Kelvin force scales with $\nabla(B^2)$ and not with the absolute field B. The order of magnitude of the magnetic gradients of 10^3 $\mathrm{T}^2\,\mathrm{m}^{-1}$ follows from the objective of having a magnetic Froude number $Fr_m = a_{\mathrm{mag}}/a_{\mathrm{flame}}$ of order one. This number compares the acceleration induced by the Kelvin force to the characteristic flame acceleration. The flame acceleration scale is defined as $a_{\mathrm{flame}} = s_L^2/\delta_f$, where s_L is the laminar flame speed obtained from the corresponding one-dimensional unstretched flame calculation. The magnetic acceleration scale is $a_{\mathrm{mag}} = \left(\chi_{\mathrm{mix}}/(2\mu_0)\right)|\nabla(B^2)|$, evaluated on the reactant side, where χ_{mix} is the mixture magnetic susceptibility, defined as the composition-weighted sum of species susceptibilities. Gravity is neglected here to isolate the effect of the imposed magnetic-field gradient. The magnetic acceleration considered in the present cases is about one to two orders of magnitude larger than gravity, so the gravitational effects are not expected to alter the results.

Although gradients of this order may appear impractical from an engineering standpoint, macroscale hybrid magnets used for magnetic levitation and gravity compensation have reported $B\,\mathrm{d}B/\mathrm{d}z$ values of order 10^3 $\mathrm{T}^2\,\mathrm{m}^{-1}$, corresponding to $\mathrm{d}(B^2)/\mathrm{d}z$ of the same order as the gradients considered in the present work [33,34]. This indicates that gradients of order $|\nabla(B^2)| \sim 10^3$ $\mathrm{T}^2\,\mathrm{m}^{-1}$ are physically realisable in specialised high-field laboratory facilities. However, achieving such conditions currently requires dedicated large-scale magnet infrastructures with substantial power and cooling demands. The present gradient range should therefore be interpreted as a proof-of-physics range for identifying the magnetic suppression mechanism, rather than as a level presently compatible with direct integration into practical combustors. Even higher gradients have also been reported for other specialised applications [35]. In the linear-regime analysis, the flame is initialised with a sinusoidal perturbation of amplitude $A = 10^{-3}\delta_f$, whereas in the nonlinear-regime analysis a larger sinusoidal perturbation with amplitude $A > 3\delta_f$ is imposed, as shown in Fig. 1. A summary of all cases performed is provided in Table 1.

2.3. Validation

In order to assess the capability of our *in-house* solver to correctly predict the influence of magnetic conditioning on reacting flows, the laminar oxy-fuel diffusion-flame studied experimentally and numerically by Yamada et al. [13,32] is chosen as test case to benchmark numerical results. This case and associated details are shown in Fig. 2. Note that part of the results for this case were already presented in our previous study [19], where comparison with available experimental observations was also discussed, and the reader is referred to that work for a more comprehensive overview of numerical and simulation details. In this oxy-fuel configuration the applied magnetic field reaches

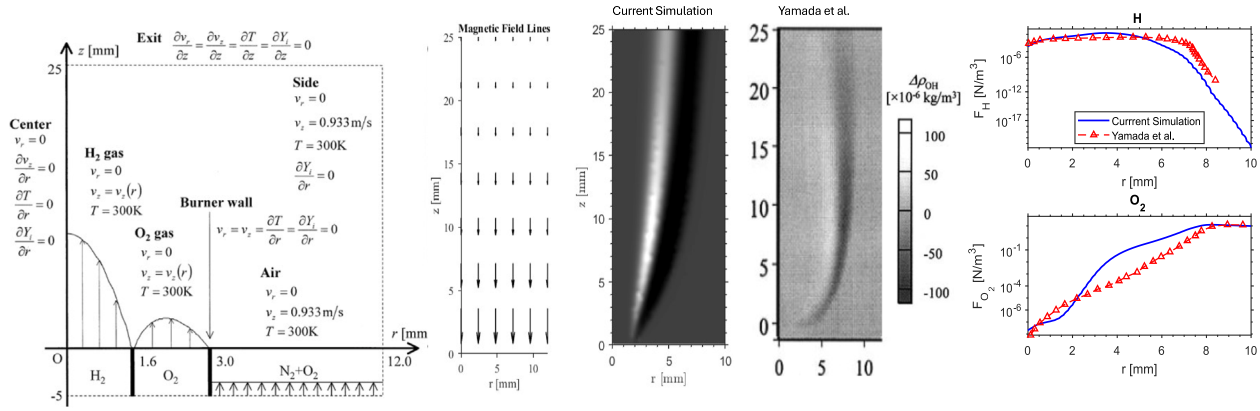

Fig. 2. Sketch of the numerical domain showing inlet and boundary conditions together with the imposed magnetic field lines (left). Comparison of OH concentration difference contours between the cases with and without magnetic fields from numerical simulations [32] and the present computations, along with the radial distribution of the magnetic body-force density acting on H and O_2 at $z = 10$ mm (right).

Table 1
Summary of simulated cases and corresponding averaged flame properties. Here, s_c/s_L is the consumption speed normalised by the laminar flame speed, Σ/A_0 is the normalised flame surface, and I is the stretch factor. The laminar flame speed is $s_L = 20.5$ cm/s for the DLI+TDI cases and $s_L = 42.1$ cm/s for the DLI-only cases.

Case	$\lvert\nabla(B^2)\rvert$ [T^2 m^{-1}]	Instability type	Fr_m	s_c/s_L	Σ/A_0	I
1	0	DLI+TDI	0.0	4.20	2.10	1.99
2	−1000	DLI+TDI	1.3	4.05	2.03	1.99
3	−2000	DLI+TDI	2.7	3.71	1.87	1.98
4	+2000	DLI+TDI	2.7	4.73	2.35	2.01
5	−3000	DLI+TDI	4.1	3.27	1.67	1.96
6	0	DLI	0.0	1.42	1.38	1.03
7	−1000	DLI	0.4	1.21	1.16	1.03
8	+1000	DLI	0.4	1.71	1.58	1.04
9	−2000	DLI	0.8	1.02	1.01	1.01

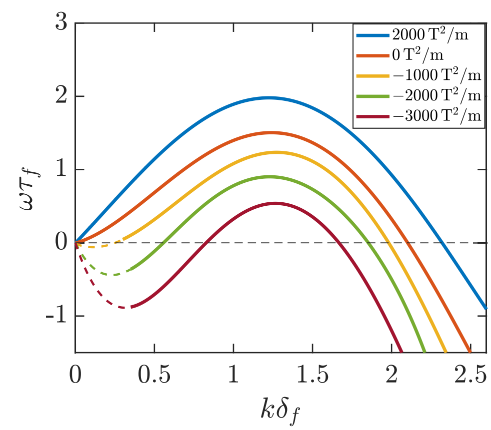

Fig. 3. Dispersion relation in the linear regime for different imposed magnetic-field gradients (Cases 1–5).

$B \approx 0.52$ T near the nozzle exit and decays exponentially downstream, resulting in a negative axial $\nabla(B^2)$. The associated Kelvin forcing acts against the streamwise transport of paramagnetic species, most notably O_2 and OH, and produces a measurable reorganisation of radicals and heat release, which can be observed by the difference $\Delta\rho_{OH}$ between the OH concentration in the cases with and without magnetic field (Fig. 2, centre). The field of OH-concentration differences predicted by our numerical approach captures the displacement observed experimentally under magnetic forcing and follows the trends reported in the literature simulations. In addition, radial profiles of the magnetic body-force density acting on H and O_2 at an axial distance from the burner mouth $z = 10$ mm, also shown in Fig. 2 (right), agree well with numerical results in [32]. These comparisons suggest that the numerical approach used here is able to capture the correct trends of flame behaviour under the influence of magnetic conditioning. Together with the experimental comparisons discussed in our previous work [19], this supports the present Kelvin-force-based interpretation of the magnetic-field effect.

3. Results

3.1. Linear regime

The influence of the imposed magnetic-field gradient is first examined in the linear regime through the corresponding dispersion relation. Following the standard approach for intrinsic-instability analyses, the flame front is initialised with a weak harmonic perturbation of wavenumber k, and the exponential growth rate ω is determined from the temporal evolution of the perturbation amplitude $A(t)$ as

$$\omega = \frac{\mathrm{d}\ln A(t)}{\mathrm{d}t}. \tag{9}$$

In the following, the dispersion relation is presented in nondimensional form as $\omega\tau_f$ versus $k\delta_f$, where $\tau_f = \delta_f/s_L$ is the characteristic flame time. Fig. 3 shows that the imposed magnetic-field gradient modifies the dispersion relation in a clear and systematic manner. A positive gradient shifts the curve upward and increases the peak growth rate, whereas negative gradients progressively reduce both the growth rate and the unstable wavenumber range. The effect is particularly pronounced at low wavenumbers, where the dispersion relation is most closely associated with the large-scale hydrodynamic response of the flame. In the absence of magnetic forcing, the growth rate remains positive in this range, indicating amplification of long-wave perturbations. A positive gradient strengthens this response, while a sufficiently strong negative gradient weakens it and stabilises part of the long-wavelength branch.

The very-low-wavenumber branch of the dispersion relation is not resolved directly by the present simulations. However, as $k \to 0$, the perturbation wavelength becomes infinite, and the disturbance approaches a uniform displacement of the planar flame, rather than a growing corrugation. The dispersion relation must therefore satisfy $\omega \to 0$ as $k \to 0$. The extrapolated connection to the origin in Fig. 3 is consistent with the analytical body-force dispersion relation derived by Matsue and Matalon [36]. Their analysis shows that the classical Darrieus–Landau contribution varies linearly with k, whereas the body-force contribution introduces a square-root dependence near $k = 0$. For a stabilising orientation of the body force, this low-wavenumber contribution shifts the branch toward the stable side.

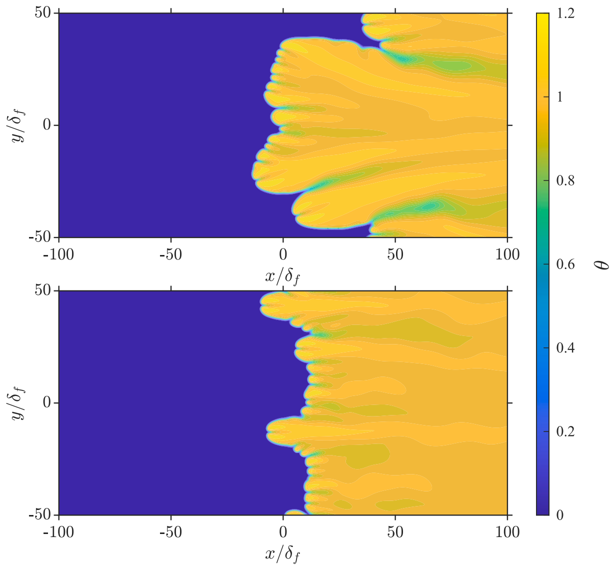

Fig. 4. Contours of normalised temperatures $\theta = (T - T_u)/(T_{ad} - T_u)$, where T_u and T_{ad} are the unburnt gas and adiabatic flame temperature, respectively, for Case 1 (top) and Case 5 (bottom) of Table 1.

At larger wavenumbers, the DL mechanism becomes dominant, and the branch returns toward positive growth rates. The resulting change in concavity reflects the exchange of dominance between the body-force-controlled long-wavelength response and the DL instability. The dotted portions in Fig. 3 therefore represent an inferred trend toward $(k, \omega) = (0, 0)$. Related linear-stability analyses for body-force effects have also been reported in the literature [37,38]. These results show that the magnetic field modifies perturbation growth already in the linear regime, before the nonlinear flame-front reorganisation discussed in the next section.

3.2. Nonlinear regime

For sufficiently large perturbation amplitudes, the flame evolves into a fully developed regime in which finite-amplitude wrinkling and cell interaction govern the flame dynamics. To identify whether the observed changes in global propagation are primarily associated with hydrodynamic (DLI) or thermodiffusive (TDI) effects, the global fuel consumption speed is expressed in the normalised form

$$\frac{s_c}{s_L} = I\,\frac{\Sigma}{A_0}, \tag{10}$$

following Berger et al. [27]. Here, Σ denotes the flame surface (per unit out-of-plane length in 2D), A_0 is the cross-sectional area, Σ/A_0 is the global wrinkling factor, and I is the stretch factor that accounts for variations in local flame reactivity. The averaged values of s_c/s_L, Σ/A_0, and I for all cases are reported in Table 1. It should be noted that the DLI+TDI and DLI-only cases are normalised with the laminar flame speed of their respective one-dimensional reference flames. Since imposing $Le_i = 1$ changes the planar laminar flame solution, using a single common s_L would affect the partition between Σ/A_0 and I in Eq. (10) and make the comparison less consistent.

For the cases where both TDI and DLI are present (Cases 1–5), applying the magnetic-field gradient in the streamwise direction (negative sign) reduces flame surface and consumption speed, while reversing the direction increases them. Relative to the zero-gradient baseline (Case 1), the case with the strongest negative gradient (Case 5) shows about a 22% reduction in the wrinkling component of the consumption speed. Note that the stretch factor remains nearly constant across these cases, suggesting that the magnetic gradient is only affecting the flame topology and not the flame internal structure. Similar observations can be made for the cases where only the DLI is present (Cases 6–9, Le = 1), with the only difference that the stretch factor is about 1 for these cases. This is due to the fact that the local flame reactivity is affected by the coupling between stretch and differential diffusion, and this coupling is suppressed for the cases at Le = 1.

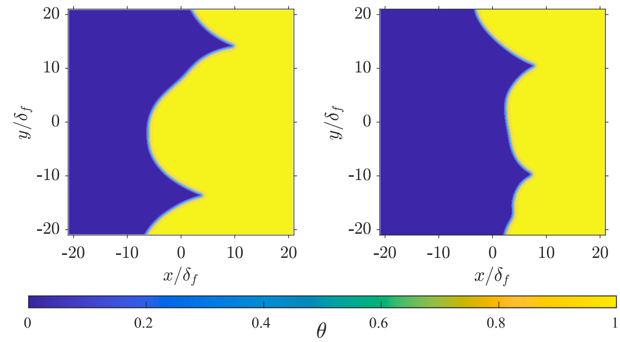

Fig. 5. Contours of normalised temperature θ for Case 6 (left) and Case 7 (right) of Table 1.

Normalised temperature contours are shown in Fig. 4 for the cases without (Case 1) and with (Case 5) magnetic gradient. The case with a negative magnetic gradient shows visibly reduced large-scale front corrugation compared with the baseline case without magnetic forcing. However, the peak (super-adiabatic) temperature levels remain essentially unchanged in both cases. This qualitative reduction in wrinkling at the large scales is consistent with the lower Σ/A_0 and s_c/s_L and the near-constant I observed in Table 1, and suggests that the DLI is affected by the magnetic gradient, while the TDI is largely unaffected. A similar reduction in wrinkling is observed in the DLI-only configuration shown in Fig. 5, again without a noticeable change in the stretch factor. This further indicates the effectiveness of the magnetic gradient in suppressing the DLI.

To shed more light on this, the flame front is analysed as follows. A progress variable is defined as $c = 1 - Y_{H_2}/Y_{H_2,u}$, where Y_{H_2} and $Y_{H_2,u}$ are the hydrogen mass fraction and its value in the fresh reactants, respectively. The isoline $c = 0.8$ is then chosen to represent the flame front, and its flame surface Σ is mapped against the isoline arc-length coordinate ℓ. The flame surface signal, $\Sigma(\ell)$, is then decomposed into large and small scales by applying a wavelength cutoff tied to the characteristic cell size. Scales with $\lambda_{\mathrm{DL}} > \lambda_{\mathrm{cutoff}}$ are classified as large-scale (DLI-related), and scales with $\lambda_{\mathrm{TD}} < \lambda_{\mathrm{cutoff}}$ are classified as small-scale (TDI-related). The resulting contributions, Σ_{DL} (large scales) and Σ_{TD} (small scales), quantify how much each range of λ adds to overall wrinkling. The same procedure is applied to all cases of Table 1, so that changes in s_c/s_L can be associated with either large- or small-scale surface content. The results of this scale separation are illustrated in Fig. 6 for the baseline case (left) and the negative streamwise gradient case (right). For the baseline (Case 1), the $c = 0.8$ isoline displays coexisting large undulations and fine cellular structure. An intermediate feature, the flame finger, appears with a characteristic spacing of about $6\,\delta_f$, which supports the choice $\lambda_{\mathrm{cutoff}} \approx \lambda_{\mathrm{cell}} \approx 6\,\delta_f$ [39]. For the negative streamwise gradient case (Case 5), the flame front is observed to span a shorter distance in the streamwise direction as compared to the case without magnetic gradient. The corresponding flame surface for Cases 1 and 5 is reported in Table 2 (normalised by the laminar flame thickness δ_f). The total flame surface decreases in Case 5 by approximately 24% as compared to Case 1. As one can observe from the table, this reduction is almost entirely due to the large-scale contribution Σ_{DL}, whereas the small-scale contribution remains essentially unchanged between the two cases, which further confirms the observation that the change in s_c/s_L (see also Table 1) indicates

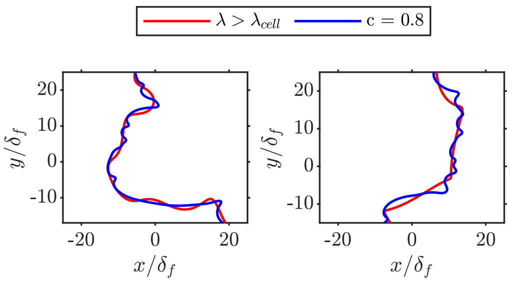

Fig. 6. Flame front represented by the isoline $c = 0.8$ (blue lines), and its reconstruction (red lines) obtained by filtering out the small scales with cutoff wavelength $\lambda_{\text{cell}} = 6\delta_f$. Left: Case 1 of Table 1; Right: Case 5 of Table 1.

Table 2
Normalised flame surface and its contributions at the large (Σ_{DL}) and small (Σ_{TD}) scales.

Case	Σ/δ_f	$\Sigma_{\text{DL}}/\delta_f$	$\Sigma_{\text{TD}}/\delta_f$
1 (no field)	138.05	121.10	16.95
5 (negative gradient)	101.30	84.99	16.40

that the magnetic-field gradient suppresses flame wrinkling primarily through its effect on the DLI.

It is also useful to examine flame-front curvature κ as a qualitative indicator of the relative contributions of large- and small-scale wrinkling. Fine cellular structures are associated with high local curvature, whereas long-wavelength undulations generally correspond to lower curvature magnitudes. The probability density function (PDF) of flame-front curvature is therefore evaluated for the baseline case without magnetic forcing (Case 1) and for the negative-gradient case (Case 5), as shown in Fig. 7.

In both cases, the distribution peaks at positive curvature. Under the negative magnetic-field gradient, the peak probability increases slightly, and the tails at larger curvature magnitudes become more pronounced. This behaviour is consistent with the scale-decomposed flame-surface analysis, as the large-scale wrinkle component is reduced, the curvature statistics become increasingly dominated by the remaining small-scale cellular structures, which populate the higher-curvature range. The PDF of curvature, therefore, provides further evidence that the imposed magnetic-field gradient selectively suppresses the large-scale component of intrinsic flame wrinkling while leaving the finer cellular structures comparatively persistent. The remaining question is therefore which physical mechanism allows the magnetic-field gradient to attenuate primarily the large-scale hydrodynamic corrugation of the flame, which is investigated next.

An imposed magnetic-field gradient may affect the flame through two distinct pathways. It acts directly on the flow as a body force in the momentum equation, and, because the Kelvin force is species dependent, it may also induce a force-driven drift contribution to species transport. The importance of this second pathway is assessed by comparing the magnetic-drift flux with the baseline molecular-diffusion flux and with thermal diffusion, which is known to be important in lean hydrogen flames.

Fig. 8 reports the conditional means of the magnitudes of the different flux contributions of all the paramagnetic species as a function of the progress variable c. For all species, molecular diffusion is the dominant transport mechanism and reaches its largest values across the reaction zone. The highest levels are found for O_2, with magnitudes of order 10^{-2}, followed by OH and O, which remain of order 10^{-3}. Lower levels are observed for H, of order 10^{-4}, and for HO_2, of order 10^{-5}. For H, the thermal-diffusion contribution reaches order 10^{-5}, i.e. within one order of magnitude of the molecular-diffusion level, confirming that Soret transport remains relevant under the present lean-hydrogen conditions. By contrast, the magnetic-drift contribution is several orders

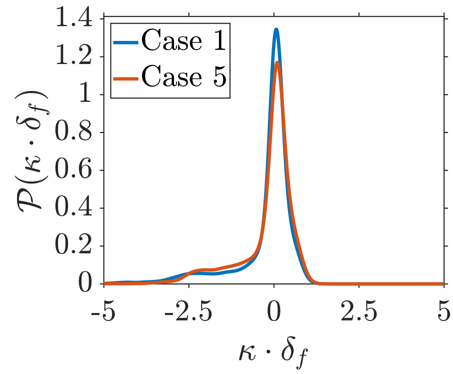

Fig. 7. Comparison of the probability density function (PDF) of flame-front curvature between the baseline case without magnetic gradient (Case 1) and the case with a negative magnetic gradient (Case 5).

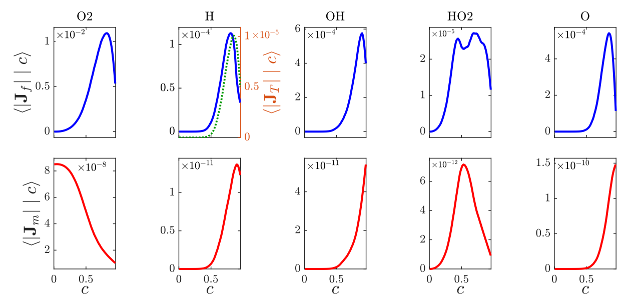

Fig. 8. Conditional means of the magnitudes of diffusive flux contributions as a function of the progress variable c. Top row: Fickian diffusion $\langle |J_f| \mid c\rangle$ for O_2, H, OH, HO_2, and O; for H, the Soret (thermal-diffusion) contribution $\langle |J_T| \mid c\rangle$ is also shown (green dotted line). Bottom row: magnetic drift contribution $\langle |J_m| \mid c\rangle$ for the same paramagnetic species.

of magnitude smaller for all species. Its largest value is found for oxygen, but it remains only of order 10^{-8}, while OH and O remain around 10^{-10}, and H and HO_2 around 10^{-11}. The direct contribution of magnetic drift to species transport is therefore negligible compared with molecular diffusion and, for hydrogen flames, also with thermal diffusion. This indicates that the magnetic-field gradient does not influence the flame through a direct modification of species transport. The discussion, therefore, focuses on the momentum pathway, where the magnetic body force alters the flow field and, in turn, the flame-front kinematics and development of hydrodynamic instability.

To understand why a negative magnetic-field gradient preferentially suppresses large-scale wrinkling, it is helpful to recall the mechanism of the hydrodynamic instability. Consider a nearly planar premixed flame perturbed by a weak long-wavelength corrugation. Heat release across the front produces a strong density drop, which accelerates the flow through the reaction zone. When the front is corrugated, this acceleration is non-uniform along the interface, generating a tangential velocity jump across the flame that behaves as a distributed vortex sheet. The velocity field induced by this sheet amplifies the perturbation: bulges are driven further into the products, while troughs are pulled back toward the reactants, leading to the growth of large-scale wrinkles [40]. Under a negative $\nabla(B^2)$, the magnetic body force is concentrated near the flame because both density and mixture magnetic susceptibility vary sharply across the reaction zone. Owing to Curie's law, χ_{mix} is larger in the colder, oxygen-rich reactants than in the hotter products, so the magnetic forcing is stronger upstream than downstream. This produces a cross-flame force imbalance that varies along a wrinkled interface. The resulting flow response induces transverse motion that opposes, at least partly, the lateral motion associated with hydrodynamic wrinkle growth. As a result, the flame front remains closer to its

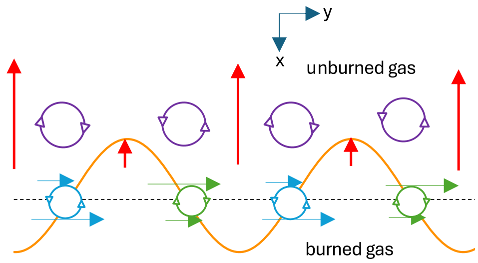

Fig. 9. Schematic of a perturbed flame front under the action of DLI and negative magnetic gradient. Blue and green arrows indicate the transverse velocity jump causing the surface growth. Red arrows indicate the magnetic body force. Purple arrows show the counter-rotating vortices created by the magnetic gradient, which weaken the DLI.

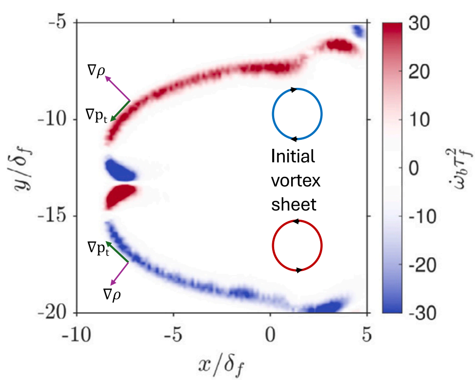

Fig. 10. Contour of normalised baroclinic torque near a wrinkled premixed flame. The two circular markers indicate the vortices used to perturb the flame. ∇p_t denotes the tangential component of pressure gradient along the flame surface; $\nabla \rho$ denotes the density gradient across the flame.

mean position, thereby reducing the amplification of long-wavelength wrinkles, as sketched in Fig. 9.

An equivalent way to describe the same hydrodynamic response is through the baroclinic vorticity generated by a wrinkled premixed flame. Once the front becomes corrugated, the pressure field also becomes non-uniform along the interface. As a result, the pressure gradient is no longer purely normal to the flame surface [41]. A tangential component develops along the front, while the density gradient remains predominantly oriented across the flame. The misalignment of these two gradients generates baroclinic torque, which acts as an additional source of vorticity localised within the flame zone. The corresponding baroclinic vorticity production rate is

$$\dot{\omega}_b \equiv \frac{\nabla \rho \times \nabla p}{\rho^2}. \tag{11}$$

Fig. 10 illustrates this mechanism. On oppositely sloped segments of a wrinkle, the sign of $\dot{\omega}_b$ changes, leading to the generation of a counter-rotating vorticity pair adjacent to the flame. The transverse velocity induced by this pair opposes the lateral motion responsible for the DLI growth and therefore provides a restoring tendency. As the wrinkle amplitude increases, the pressure difference between crests and troughs also increases, which strengthens the tangential pressure gradient and enhances baroclinic vorticity production. The wrinkle therefore tends toward a finite amplitude once the instability-driven amplification is balanced by the opposing baroclinic response. This interpretation is consistent with earlier analyses of curved density interfaces subjected to differential body forcing, where modification of the local pressure field changes the baroclinic vorticity induced at the interface [37,42]. In the present case, the magnetic-field gradient alters this competition by reshaping the pressure field in the immediate

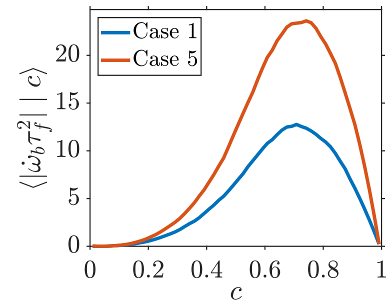

Fig. 11. Conditional mean of the magnitude of the non-dimensional baroclinic vorticity source, $\langle|\dot{\omega}_b \tau_f^2| \mid c\rangle$, as a function of progress variable c for Case 1 (no magnetic field) and Case 5 (negative magnetic-field gradient).

vicinity of the flame. Because the Kelvin force is stronger in the colder reactants than in the hotter products, it introduces an additional cross-flame pressure variation across the reaction zone. When the flame is curved, this contribution becomes non-uniform along the interface and reinforces the pressure difference between crests and troughs. The tangential component of the pressure gradient along the flame surface therefore increases, the misalignment between ∇p and the cross-flame density gradient becomes stronger, and baroclinic vorticity production intensifies. The resulting counter-rotating vorticity near the flame is strengthened, so the induced transverse motion more effectively opposes the lateral flow that amplifies long-wavelength wrinkles. Fig. 11 supports this interpretation. The conditional mean $\langle|\dot{\omega}_b \tau_f^2| \mid c\rangle$ peaks within the reactive layer, consistent with baroclinic production being concentrated where the density gradient is strongest. Compared with the no-field case, the negative-gradient case exhibits higher levels across most of the reaction zone and a larger peak value, indicating enhanced baroclinic activity in the flame region. This provides a direct mechanistic link between the imposed magnetic-field gradient and the observed reduction in large-scale flame wrinkling: the field does not suppress the instability through species-transport effects, but by strengthening the baroclinic restoring response that counteracts hydrodynamic Darrieus–Landau growth. Small-scale cellular structures, which are instead more associated with local transport imbalance and differential diffusion, can therefore persist even as the large-scale hydrodynamic corrugation is attenuated.

4. Conclusion

Two-dimensional high-fidelity simulations have been performed for lean premixed, freely propagating hydrogen flames subjected to both Darrieus–Landau (DL) and thermodiffusive (TD) instabilities. Magnetic-field gradients of different magnitudes and orientations have been systematically imposed within a two-dimensional magnetostatic Kelvin-force framework to isolate their effect on intrinsic flame-instability dynamics. Results show that a negative streamwise magnetic-field gradient reduces the growth of perturbations already in the linear regime by weakening the long-wavelength branch of the dispersion relation, and correspondingly damps wrinkling in the fully developed flame, thereby reducing the consumption speed. Minimal change was observed in the flame stretch factor and superadiabatic temperature, indicating that the effect on flame structure and reactivity is negligible. Further analysis of the flame surface indicates that the magnetic forcing primarily suppresses the DL instability. The mechanism is associated with vortical structures generated by the density and susceptibility jump across the flame, which oppose the surface growth driven by gas expansion. Overall, the present results provide a physics-based demonstration that externally imposed magnetic-field gradients can alter the development of intrinsic instabilities in premixed hydrogen flames.

CRediT authorship contribution statement

Vaibhav Mysore Natesh: Writing – review & editing, Writing – original draft, Methodology, Investigation, Formal analysis. **Ivan Langella:** Writing – review & editing, Supervision, Funding acquisition, Conceptualization.

Declaration of competing interest

The authors declare that they have no known competing financial interests or personal relationships that could have appeared to influence the work reported in this paper.

Acknowledgements

This project has received funding from the European Union's Horizon Europe Research and Innovation Programme under grant agreement No. 101120321, project ICHAruS. This work used the Dutch national e-infrastructure with the support of the SURF Cooperative, using grant no. EINF-14229. The authors acknowledge Vittorio De Lauso for his major contribution to the development of the in-house version of the reactingFOAM code.

References

[1] T. Capurso, D. Laera, É. Riber, B. Cuenot, NO_x pathways in lean partially premixed swirling H_2-air turbulent flame, Combust. Flame 248 (2023) 112581.
[2] H. Pitsch, The transition to sustainable combustion: Hydrogen-and carbon-based future fuels and methods for dealing with their challenges, Proc. Combust. Inst. 40 (1–4) (2024) 105638.
[3] L. Berger, A. Attili, H. Pitsch, Synergistic interactions of thermodiffusive instabilities and turbulence in lean hydrogen flames, Combust. Flame 244 (2022) 112254.
[4] K.R. McManus, T. Poinsot, S. Candel, A review of active control of combustion instabilities, Prog. Energy Combust. Sci. 19 (1) (1993) 1–29, http://dx.doi.org/10.1016/0360-1285(93)90020-F.
[5] T.C. Lieuwen, V. Yang (Eds.), Combustion Instabilities in Gas Turbine Engines: Operational Experience, Fundamental Mechanisms, and Modeling, in: Progress in Astronautics and Aeronautics, vol. 210, American Institute of Aeronautics and Astronautics (AIAA), Reston, VA, 2005.
[6] A. Starikovskiy, N. Aleksandrov, Plasma-assisted ignition and combustion, Prog. Energy Combust. Sci. 39 (2013) 61–110, http://dx.doi.org/10.1016/j.pecs.2012.05.003.
[7] Y. Ju, W. Sun, Plasma assisted combustion: Dynamics and chemistry, Prog. Energy Combust. Sci. 48 (2015) 21–83, http://dx.doi.org/10.1016/j.pecs.2014.12.002.
[8] J. Sun, Y. Tang, S. Li, Plasma-assisted stabilization of premixed swirl flames by gliding arc discharges, Proc. Combust. Inst. 38 (4) (2021) 6733–6741, http://dx.doi.org/10.1016/j.proci.2020.06.223.
[9] T. Poinsot, D. Veynante, Theoretical and Numerical Combustion, second ed., R. T. Edwards, Inc., 2005.
[10] A. Porcarelli, P.E. Lapenna, F. Creta, I. Langella, Stability analysis of thermodiffusively unstable counterflow lean premixed hydrogen flames, Proc. Combust. Inst. 41 (2025) 105906.
[11] R. Concetti, J. Hasslberger, M. Klein, Direct numerical simulations with multistep chemistry of liquid water interaction with laminar spherically expanding premixed hydrogen/air flames, Int. J. Hydrog. Energy 115 (2025) 10–23.
[12] I.S. Yakovenko, A.D. Kiverin, Intensification mechanisms of the lean hydrogen-air combustion via addition of suspended micro-droplets of water, Int. J. Hydrog. Energy 46 (2021) 1259–1272.
[13] E. Yamada, M. Shinoda, H. Yamashita, K. Kitagawa, Experimental and numerical analyses of magnetic effect on OH radical distribution in a hydrogen-oxygen diffusion flame, Combust. Flame 135 (4) (2003) 365–379.
[14] O. Fjita, K. Ito, T. Chida, S. Nagai, Y. Takeshita, Determination of magnetic field effects on a jet diffusion flame in a microgravity environment, Symp. (International) Combust. 27 (2) (1998) 2573–2578.
[15] S. Ueno, K. Harada, Effects of magnetic fields on flames and gas flow, IEEE Trans. Magn. 23 (5) (1987) 2752–2754, http://dx.doi.org/10.1109/TMAG.1987.1065242.
[16] T. Kajimoto, E. Yamada, M. Shinoda, K. Kitagawa, Dependence of magnetically induced change in OH distribution in a methane-air premixed flame on equivalence ratio, Combust. Sci. Technol. 175 (9) (2003) 1611–1623.
[17] M. Shinoda, E. Yamada, T. Kajimoto, H. Yamashita, K. Kitagawa, Mechanism of magnetic field effect on OH density distribution in a methane–air premixed jet flame, Proc. Combust. Inst. 30 (1) (2005) 277–284, http://dx.doi.org/10.1016/j.proci.2004.07.006.
[18] A. Porcarelli, B. Kruljević, I. Langella, Suppression of NOx emissions by intensive strain in lean premixed hydrogen flamelets, Int. J. Hydrog. Energy 49 (2024) 413–431.
[19] V.M. Natesh, I. Langella, Influence of magnetic field on flame dynamics in hydrogen flames: A numerical study, Proc. Combust. Inst. 41 (2025) 105892.
[20] E.M. Kritikos, S. Cant, A. Giusti, A computational approach for the study of electromagnetic interactions in reacting flows, 2025, http://dx.doi.org/10.48550/arXiv.2505.06433, arXiv:2505.06433.
[21] K. Schofield, The enigmatic mechanism of the flame ionization detector: Its overlooked implications for fossil fuel combustion modeling, Prog. Energy Combust. Sci. 34 (3) (2008) 330–350, http://dx.doi.org/10.1016/j.pecs.2007.08.001.
[22] J.A. Green, T.M. Sugden, Some observations on the mechanism of ionization in flames containing hydrocarbons, in: Symposium (International) on Combustion, Vol. 9, 1963, pp. 607–621, http://dx.doi.org/10.1016/S0082-0784(63)80070-3.
[23] T. Aoki, Radicals' emissions and butane diffusion flames exposed to upward-decreasing magnetic fields, Japan. J. Appl. Phys. 28 (5R) (1989) 776–785, http://dx.doi.org/10.1143/JJAP.28.776.
[24] V. De Lauso, L. Mazzei, I. Langella, Flame control by low-temperature hydrogen injection in a trapped vortex combustor, Proc. Combust. Inst. 41 (2025) 105865, http://dx.doi.org/10.1016/j.proci.2025.105865.
[25] L. Berger, A. Attili, H. Pitsch, Intrinsic instabilities in premixed hydrogen flames: Parametric variation of pressure, equivalence ratio, and temperature. Part 1 - dispersion relations in the linear regime, Combust. Flame 240 (2022) 111935, http://dx.doi.org/10.1016/j.combustflame.2021.111935.
[26] S.A. Kassar, R. Lamioni, I. Langella, F. Creta, Efficient and accurate calculation of dispersion relations for intrinsic flame instabilities with a single simulation, Combust. Flame 267 (2024) 113603, http://dx.doi.org/10.1016/j.combustflame.2024.113603.
[27] L. Berger, A. Attili, H. Pitsch, Intrinsic instabilities in premixed hydrogen flames: parametric variation of pressure, equivalence ratio, and temperature. Part 2–non-linear regime and flame speed enhancement, Combust. Flame 240 (2022) 111936.
[28] L. Berger, K. Kleinheinz, A. Attili, H. Pitsch, Characteristic patterns of thermodiffusively unstable premixed lean hydrogen flames, Proc. Combust. Inst. 37 (2) (2019) 1879–1886.
[29] M.P. Burke, M. Chaos, Y. Ju, F.L. Dryer, S.J. Klippenstein, Comprehensive H_2/O_2 kinetic model for high-pressure combustion, Int. J. Chem. Kinet. 44 (7) (2012) 444–474.
[30] J. Schlup, G. Blanquart, Validation of a mixture-averaged thermal diffusion model for premixed lean hydrogen flames, Combust. Theory Model. 22 (2) (2018) 264–290, http://dx.doi.org/10.1080/13647830.2017.1398350.
[31] T. Zirwes, A. Kronenburg, Assessment of approximate soret diffusion models for hydrogen and ammonia combustion, Flow, Turbul. Combust. (2025) 1–20.
[32] E. Yamada, M. Shinoda, H. Yamashita, K. Kitagawa, Numerical analysis of a hydrogen-oxygen diffusion flame in vertical or horizontal gradient of magnetic field, Combust. Sci. Technol. 174 (9) (2002) 149–164.
[33] M.V. Berry, A.K. Geim, Of flying frogs and levitrons, Eur. J. Phys. 18 (4) (1997) 307–313, http://dx.doi.org/10.1088/0143-0807/18/4/012.
[34] E. Beaugnon, R. Tournier, Levitation of water and organic substances in high static magnetic fields, J. de Phys. I 1 (11) (1991) 1423–1428, http://dx.doi.org/10.1051/jp1:1991184.
[35] V. Nikolayev, D. Chatain, D. Beysens, G. Pichavant, Magnetic gravity compensation, 2018, arXiv preprint arXiv:1804.03838 URL https://arxiv.org/abs/1804.03838.
[36] K. Matsue, M. Matalon, Hydrodynamically unstable premixed flames in gravitational fields: Effect of gas expansion, Combust. Flame 281 (2025) 114403, http://dx.doi.org/10.1016/j.combustflame.2025.114403.
[37] K.-L. Pan, Transformation of premixed flame behavior with hydrodynamic and body-force instabilities, Phys. Fluids 20 (4) (2008) 044106.
[38] J. Zheng, H. Wang, K. Luo, J. Fan, The stability and morphology of laminar premixed hydrogen/air flames under various gravity conditions, Combust. Flame 267 (2024) 113602, http://dx.doi.org/10.1016/j.combustflame.2024.113602.
[39] L. Berger, M. Grinberg, B. Jürgens, P.E. Lapenna, F. Creta, A. Attili, H. Pitsch, Flame fingers and interactions of hydrodynamic and thermodiffusive instabilities in laminar lean hydrogen flames, Proc. Combust. Inst. 39 (2) (2023) 1525–1534.
[40] M. Matalon, The Darrieus–Landau instability of premixed flames, Fluid Dyn. Res. 50 (5) (2018) 051412, http://dx.doi.org/10.1088/1873-7005/aab510.
[41] C.J. Mueller, J.F. Driscoll, D.L. Reuss, M.C. Drake, M.E. Rosalik, Vorticity generation and attenuation as vortices convect through a premixed flame, Combust. Flame 112 (1998) 342.
[42] J.O. Sinibaldi, C.J. Mueller, A.E. Tulkki, J.F. Driscoll, Suppression of flame wrinkling by buoyancy: The baroclinic stabilization mechanism, AIAA J. 36 (1998) 1432.